DOI: 10.1002/ejic.200600680

Crystal Structure, Solid-State NMR Spectroscopic and Photoluminescence Studies of Organic-Inorganic Hybrid Materials $(HL)_6[Ge_6(OH)_6(hedp)_6]\cdot 2(L)\cdot nH_2O$, L = hqn or phen[‡]

Luís Mafra,[a] Filipe A. Almeida Paz,[a] Fa-Nian Shi,[a] Rute A. Sá Ferreira,[b] Luís D. Carlos,[b] Tito Trindade,[a] Christian Fernandez,[c] Jacek Klinowski,[d] and João Rocha*[a]

Keywords: Germanium / Organic–inorganic hybrid materials / Crystal structure / NMR spectroscopy / Photoluminescence

Two germanium–$hedp^{4-}$ solids with heteroaromatic amines 8-hydroxyquinoline (hqn) and 1,10-phenanthroline (phen), $(HL)_6[Ge_6(OH)_6(hedp)_6]\cdot 2(L)\cdot nH_2O$ (L = hqn or phen), in **I** and **II** respectively, have been prepared and characterised by single-crystal XRD, thermogravimetry, FTIR and UV/Vis spectroscopy. The complex hydrogen-bond networks, particularly in compound **I**, have been studied by advanced high-resolution solid-state NMR spectroscopy that combines homonuclear recoupling techniques (two-dimensional ^{1}H-^{1}H DQF and ^{1}H-^{1}H RFDR MAS NMR) and combined rotation and multiple-pulse spectroscopy (two-dimensional ^{1}H-^{1}H FS-LG, ^{1}H-^{31}P FS-LG). The fine details of the crystal structure of **I** have been elucidated, mainly those involving the π–π stacking of 8-hydroxyquinoline and the relative orientation of adjacent such molecules. Compound **II** exhibits an emission from the lowest triplet-state energy (π–π* 0-phonon transition) of the aromatic rings at 320 nm (31250 cm^{-1}) from 14 K to room temperature. In contrast, the triplet emission of **I** at 530 nm (18868 cm^{-1}) is only detected at low temperature, because of thermally activated non-radiative mechanisms. The emission spectra of **I** and **II** display a lower-energy component with a larger life time, which results from the formation of an excimer state that originated from the π–π phenanthroline and hydroxyquinoline interactions, respectively.

Introduction

Crystalline inorganic–organic hybrid materials have been the subject of much interest because of their structural diversity, interesting properties and potential applications in areas such as catalysis, magnetism, optics, medicine, electronics, photochemistry, gas storage, and coating films.[1–12] The organic components of these hybrid materials, until recently based mainly on carboxylic acid functional groups, are at present being replaced by phosphonic acid moieties because of their higher chelating versatility and ability to direct interesting structural topologies.[9,13,14] Examples of these organic chelating molecules include *N*-(phosphonomethyl)iminodiacetic acid (H_4pmida)[15] and 1-hydroxyethane-1,1-diphosphonic acid (H_4HEDP).[16–18]

In general, the ^{1}H NMR spectra of solids suffer from homogeneous line broadening as a result of strong proton homonuclear dipolar couplings and the large concentration of protons in the materials. To circumvent this problem and to record high-resolution spectra, fast ^{1}H MAS NMR techniques and Combined Rotation and Multiple-Pulse Sequences (CRAMPS) have been used. In organic materials,[19–22] hydrogen-bond networks have been much studied by solid-state ^{1}H NMR spectroscopy, for example, by double-quantum filtered (DQF) NMR techniques.[21,23–26] However, advanced ^{1}H NMR techniques have been much less applied to the study of complex inorganic-hybrid materials.[27–29]

Here, we wish to report the synthesis, single-crystal structure and photoluminescence properties of two germanium–$hedp^{4-}$ solids with heteroaromatic amines 8-hydroxyquinoline and 1,10-phenanthroline, $(HL)_6[Ge_6(OH)_6(hedp)_6]\cdot 2(L)\cdot nH_2O$ (L = hqn or phen), in **I** and **II**, respectively, which are involved in columnar π–π stacking interactions and exhibit complex hydrogen-bond networks. The materials have been further characterised by elemental analysis, thermogravimetry and FTIR, Raman and UV/Vis spectroscopy. High-resolution solid-state NMR spectroscopy has been used to study the complex hydrogen-bond networks, particularly in compound **I**. The combination of homonuclear recoupling techniques (2D ^{1}H-^{1}H DQF,[30,31] 2D ^{1}H-^{1}H

[‡] hedp, hqn and phen stand for 1-hydroxyethylidenediphosphonic acid, 8-hydroxyquinoline and 1,10-phenanthroline, respectively.

[a] Department of Chemistry, University of Aveiro, CICECO, 3810-193 Aveiro, Portugal
Fax: +351-234-370-084
E-mail: rocha@dq.ua.pt
[b] Department of Physics, University of Aveiro, CICECO, 3810-193 Aveiro, Portugal
[c] Laboratoire Catalyse et Spectrochimie (CNRS UMR 6506), ENSICAEN and Université de Caen-Basse Normandie, 14050 Caen, France
[d] Department of Chemistry, University of Cambridge, Lensfield Road, Cambridge CB2 1EW, UK

Supporting information for this article is available on the WWW under http://www.eurjic.org or from the author.

RFDR MAS NMR[32,33]) and CRAMPS[34] (2D ^{1}H-^{1}H FS-LG, ^{1}H-^{31}P FS-LG) provided a powerful means of characterising these organic–inorganic hybrid materials.

Results and Discussion

X-ray Crystallography

The hydrothermal reaction between germanium(IV) oxide, etidronic acid (or 1-hydroxyethylidenediphosphonic acid, H_4hedp, $C_2H_8O_7P_2$) and 8-hydroxyquinoline (hqn, C_9H_7NO) or 1,10-phenanthroline (phen, $C_{12}H_8N_2$), followed by slow evaporation at ambient temperature (Experimental Section), afforded highly crystalline materials, which were formulated as $(Hhqn)_6[Ge_6(OH)_6(hedp)_6]\cdot 2(hqn)\cdot 33H_2O$ (**I**) and $(Hphen)_6[Ge_6(OH)_6(hedp)_6]\cdot 2(phen)\cdot 20H_2O$ (**II**) on the basis of single-crystal X-ray diffraction (Table 1) in combination with thermogravimetry and solid-state NMR studies.

The main structural feature, common to both compounds, is the presence of the centrosymmetric hexameric anionic $[Ge_6(\mu_2\text{-}OH)_6(C_2H_4O_7P_2)_6]^{6-}$ moiety (Figure 1), which bears some similarity with the fragment present in materials reported recently.[35] This anionic moiety is composed of three crystallographically unique Ge^{4+} centres [Ge(1), Ge(2) and Ge(3), Figure S2 in Supporting Information], each coordinated to two $hedp^{4-}$ residues (through the phosphonate moieties) and to two μ_2-bridging hydroxy groups, and exhibits $\{GeO_6\}$ in a slightly distorted octahedral coordination geometry: for both compounds, all the Ge–O bonds are in the range 1.79 to 1.91 Å (Table S3 in Supporting Information); however, the *cis* and *trans* octahedral angles range from 85.2° to 95.3° and 174.2° to 179.3°, respectively (Table S4 in Supporting Information). The centrosymmetric hexameric anionic unit described here is different in a fundamental way from that previously reported by Seifullina and collaborators.[35] Indeed, while in compounds **I** and **II**, the centre of gravity of this anionic unit is located at an inversion centre (Table 1), which necessarily requires the presence of three crystallographically unique Ge^{4+} centres, for the compounds reported by Seifullina et al., inversion arises as a combination of other symmetry elements, namely a twofold axis and a mirror plane (space group *C*2/m), and therefore only requires two single Ge^{4+} centres.[35] Consequently, the $[Ge_6(\mu_2\text{-}OH)_6(C_2H_4O_7P_2)_6]^{6-}$ moiety present in compounds **I** and **II** is more distorted than its *C*2/*m* counterpart. A possible reason for this decrease in symmetry is the significant number of strong hydrogen bonds present in **I** and **II** that involve the phosphonate groups.

In both compounds, the $hedp^{4-}$ organic residues are chelating bridging ligands, linking neighbouring Ge^{4+} centres through the two phosphonate groups, which coordinate the Ge^{4+} centres in *cis* positions (Figure 1a). The Ge···Ge internuclear distances range from ca. 3.32 to 3.50 Å (Figure 1), which is in good accord with the values reported by Seifullina and collaborators[35] (ca. 3.39–3.50 Å). Because

Table 1. Crystal data and structure refinement information for compounds **I** and **II**.

	I	**I** (after SQUEEZE)	**II**	**II** (after SQUEEZE)
Formula	$C_{84}H_{158}Ge_6N_8O_{89}P_{12}$	–	$C_{108}H_{140}Ge_6N_{16}O_{68}P_{12}$	–
Formula weight	3511.36	–	3557.54	–
Crystal system	Triclinic	–	Monoclinic	–
Space group	$P\bar{1}$	–	$P2_1/n$	–
a [Å]	16.201(3)	–	15.432(3)	–
b [Å]	16.997(3)	–	27.222(5)	–
c [Å]	17.321(4)	–	17.193(3)	–
α [°]	61.09(3)	–	–	–
β [°]	66.08(3)	–	102.94(3)	–
γ [°]	74.78(3)	–	–	–
Volume [Å^3]	3803.4(13)	–	7039(2)	–
Z	1	–	2	–
D_c [g cm^{-3}]	1.533	–	1.678	–
μ(Mo-K_α) [mm^{-1}]	1.402	–	1.507	–
F(000)	1802	–	3632	–
Crystal size [mm]	0.35 × 0.07 × 0.05	–	0.21 × 0.10 × 0.07	–
Crystal type	yellow blocks	–	yellow needles	–
θ range [°]	3.62 to 24.11	3.62 to 27.50	3.52 to 25.35	3.52 to 25.67
Data completeness	99.1%	98.1%	87.4%	87.0%
Index ranges	$-18 \le h \le 18$	$-20 \le h \le 21$	$-18 \le h \le 18$	$-18 \le h \le 18$
	$-19 \le k \le 19$	$-20 \le k \le 22$	$-30 \le k \le 32$	$-30 \le k \le 33$
	$-19 \le l \le 19$	$-22 \le l \le 22$	$-15 \le l \le 20$	$-15 \le l \le 20$
Reflections collected	30980	37902	24076	24554
Independent reflections	11985 (R_{int} = 0.0594)	17149 (R_{int} = 0.0606)	11271 (R_{int} = 0.0535)	11612 (R_{int} = 0.0495)
Final *R* indices [$I > 2\sigma(I)$]	R_1 = 0.0836	R_1 = 0.0639	R_1 = 0.0930	R_1 = 0.0952
	wR_2 = 0.2269	wR_2 = 0.1602	wR_2 = 0.2192	wR_2 = 0.2320
Final *R* indices (all data)	R_1 = 0.1314	R_1 = 0.1192	R_1 = 0.1724	R_1 = 0.1554
	wR_2 = 0.2672	wR_2 = 0.1774	wR_2 = 0.2661	wR_2 = 0.2564
Largest diff. peak and hole	1.133 and –1.086 e Å^{-3}	–	0.579 and –0.396 e Å^{-3}	–

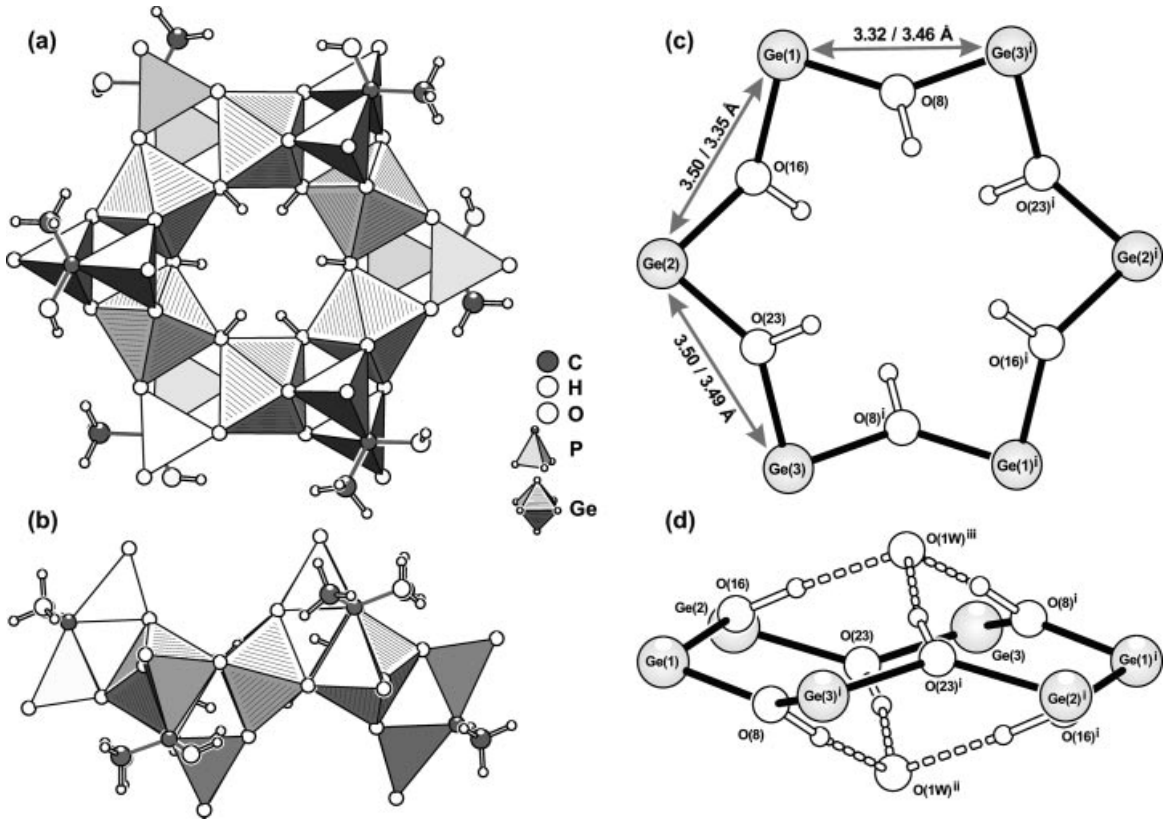

Figure 1. (a) and (b) Polyhedral representation of the hexameric anionic $[Ge_6(\mu_2\text{-}OH)_6(C_2H_4O_7P_2)_6]^{6-}$ moiety viewed from the top and from a lateral perspective. (c) and (d) Ball-and-stick representation of the internal $\{Ge_6(OH)_6\}$ hexagonal ring of the anionic $[Ge_6(OH)_6(C_2H_4O_7P_2)_6]^{6-}$ moieties. Hydrogen bonds with neighbouring O(1W) water molecules are represented as dashed lines. Selected bond lengths and angles are given in Tables S3 and S4 and the hydrogen bonding geometry in Tables S5 and S6 (Supporting Information). Symmetry codes used to generate equivalent atoms, **I**: (i) $1-x$, $2-y$, $2-z$; (ii) x, y, $1+z$; (iii) $1-x$, $2-y$, $1-z$.; **II**: (i) $1-x$, $1-y$, $2-z$; (ii) x, $-1+y$, z; (iii) $1-x$, $1-y$, $2-z$.

of steric hindrance, the six $hedp^{4-}$ ligands forming the anionic $[Ge_6(\mu_2\text{-}OH)_6(C_2H_4O_7P_2)_6]^{6-}$ moiety are distributed above and below the plane formed by the six Ge^{4+} centres (Figure 1a and Figure 1b). An identical distribution also occurs for the six μ_2-bridging hydroxy groups located and pointing towards the inner space of the hexameric moiety (Figure 1c and Figure 1d). Each one of the three μ_2-OH groups from one side of the $\{Ge_6(OH)_6\}$ hexagonal ring interacts with a neighbouring water molecule of crystallisation (Figure 1d) through strong and highly directional O–H···O hydrogen bonds [average O···O internuclear distance and <(O–H···O) angle of 2.70 Å and 163°, respectively, for both compounds, Tables S5 and S6 in Supporting Information]. Within the dihydrated anionic $[Ge_6(\mu_2\text{-}OH)_6(C_2H_4O_7P_2)_6]^{6-}$ moiety, the O(1W)···O(1W) distances are ca. 3.18 and 3.31 Å for **I** and **II**, respectively. Interestingly, such an arrangement was reported by Seifullina et al. only for the material containing $[Mg(H_2O)_6]^{2+}$ cations, with a reported corresponding distance of ca. 3.17 Å.[35] The charge of the hexameric anionic $[Ge_6(\mu_2\text{-}OH)_6(C_2H_4O_7P_2)_6]^{6-}$ moieties is compensated by the presence of protonated 8-hydroxyquinoline ($Hhqn^+$, for **I**) or 1,10-phenanthroline ($Hphen^+$, for **II**) organic residues, which appear to be π–π stacked, thus leading to the formation of cationic columnar arrangements (Figures S3 and S4 in Supporting Information): while for **I**, the organic residues alternate in a hqn/$Hhqn^+$/$Hhqn^+$ fashion, for **II**, the rod-like columns are only formed by protonated phen residues. The location of these charge-balancing H^+ could only be unequivocally confirmed in the crystal structures by solid-state NMR spectroscopy (see below). This π–π stacking arrangement of organic molecules in both compounds seems to arise mainly as a result of the presence of the relatively large hexameric anionic unit. For example, the crystal structure of pure 1,10-phenanthroline does not contain any π–π interactions, and the stacking of adjacent molecules is instead driven by numerous weak C–H···π interactions.[36] For **I**, this particular feature led to significant and interesting photoluminescence properties, as will be discussed later.

Connections between neighbouring cationic columnar arrangements are mainly assured by weak C–H···π interactions with pairs of π–π-stacked organic molecules. While for compound **I**, this distribution generates organic layers (Figure S3 in Supporting Information), for **II**, the packing is much more efficient, which leads to a three-dimensional supramolecular arrangement of phen/$Hphen^+$ residues (Figure S4 in Supporting Information). Therefore, even though compound **II** has a significantly more available volume per unit cell, the volume accessible to solvent molecules (calculated by using Cerius^2 routines[42]) is approxi-

mately half of that for **I** (Figure S5 and Table S2 in Supporting Information). These supramolecular arrangements of organic residues closely interact with the hexameric anionic $[Ge_6(\mu_2\text{-}OH)_6(C_2H_4O_7P_2)_6]^{6-}$ moieties and water molecules of crystallisation through a series of strong hydrogen bonds (Tables S5 and S6 in Supporting Information), which will be discussed in more detail in the solid-state NMR section.

As suggested by thermogravimetry and previous studies on multi-dimensional coordination frameworks exhibiting

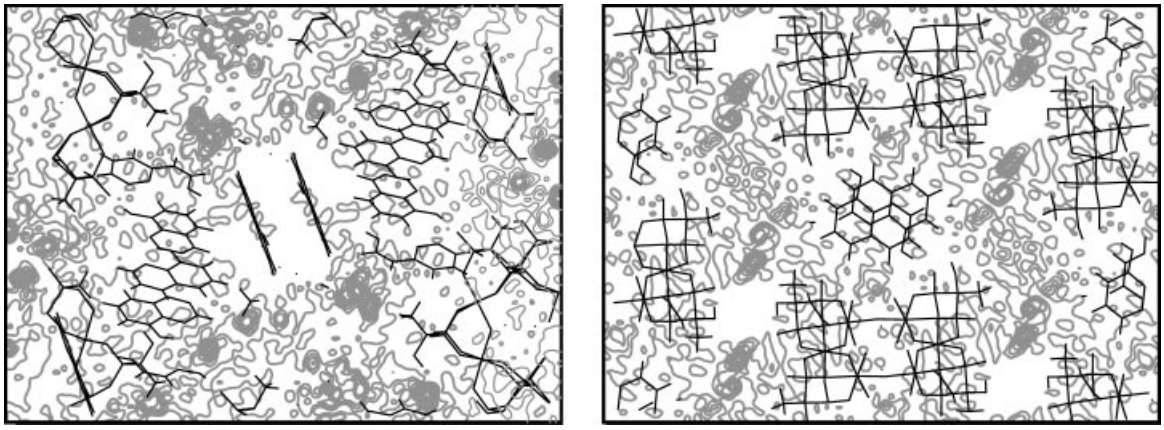

Figure 2. Contouring of difference Fourier SQUEEZE maps (grey) of compound **I** viewed parallel to the (left) *yz* and (right) *xy* planes.

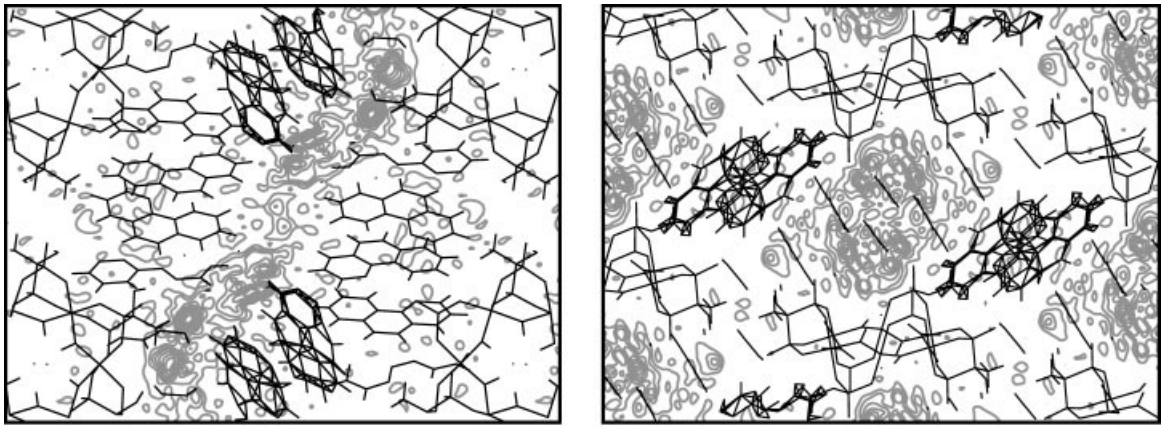

Figure 3. Contouring of difference Fourier SQUEEZE maps (grey) of compound **II** viewed parallel to the (left) *yz* and (right) *xy* planes.

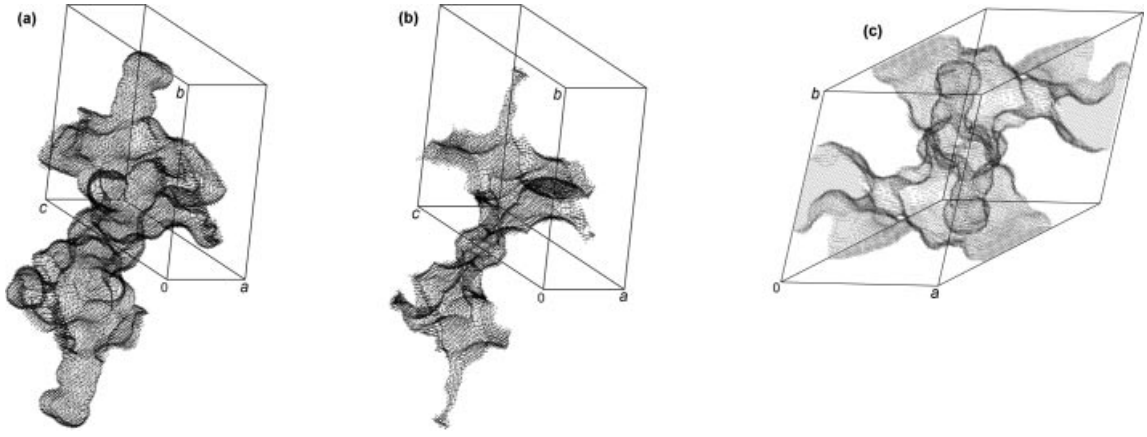

Figure 4. Solvent-accessible volumes of **I**. (a) Surface surrounding the large cavity centred at (–0.032 0.082 0.439). (b) The corresponding Ohashi volume representation showing all the points at 1.2 Å from the nearest van der Waals surface.[41] (c) Potential solvent-accessible volume inside the unit cell.

large channels,[37] it was clear that both compounds would contain a large number of highly disordered water molecules of crystallisation located within the voids, thus resulting in a significant spread-out electron density visible in the XRD data. Peak search routines of SHELXL are not designed to locate maxima in density ridges, which thus lead to additional difficulties during refinement and mask important structural features. SQUEEZE[38] subroutines included with the software package PLATON[39,40] were therefore employed to eliminate the contribution to the electron density of the water molecules of crystallisation present in the solvent-accessible area [except for the hydrogen-bonded O(1W) molecule, Figure 1c and Figure 1d]. Figure 2 and Figure 3 show the SQUEEZE contour maps for **I** and **II**, respectively, and emphasise the diffuse electron density present in some of the regions with solvent-accessible voids. For **I**, PLATON estimated that the unit cell has ca. 1363 Å^3 that is potentially accessible to the solvent (ca. 35.8% of the total volume) in a large cavity centred at (–0.032 0.082 0.439), with ca. 263 electrons per unit cell (Figure 4 and S5 in Supporting Information). For **II**, the unit cell only has ca. 1144 Å^3 that is potentially accessible to the solvent (ca. 16.3% of the total volume), which is distributed along two identical cavities centred at the special positions (0 0 0) and (1/2 1/2 1/2), with ca. 547 electrons per unit cell (Figure 5, S5 and S6 in Supporting Information). In all calculations, O(1W) was assumed to belong to the hybrid hydrogen-bonded frameworks.

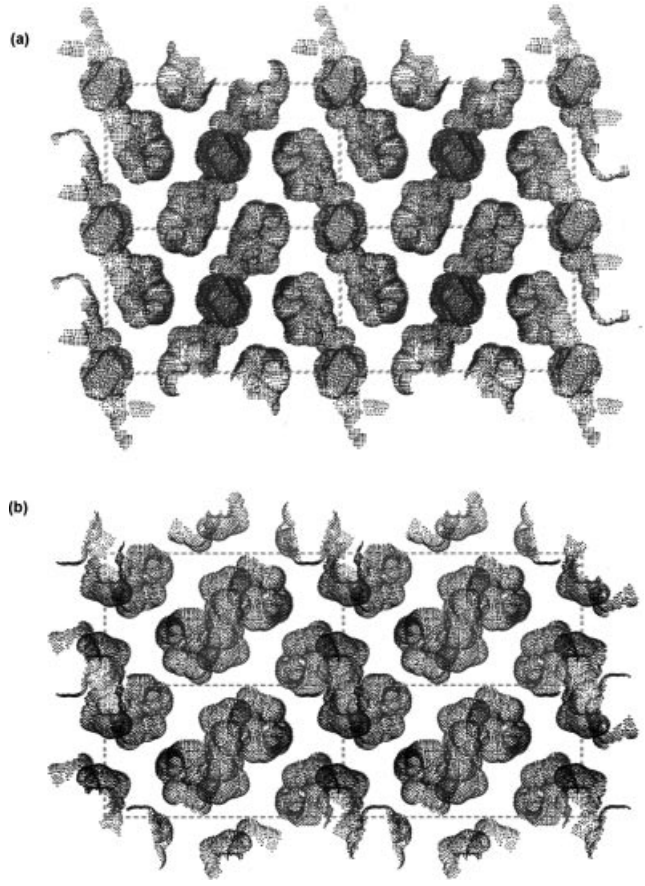

Figure 5. Perspective views along the (a) [100] and (b) [010] directions of the 2×2 unit cell packing of **II**, enhancing the shape of the two identical cavities centred at (0 0 0) and (1/2 1/2 1/2). Images created by generating Connolly surfaces (1.4 Å probe radius and 12.0 dot density) with the software package Cerius^2.[42]

Solid-State NMR Spectroscopy

^{13}C CP MAS NMR Spectra

The spectra of **I** and **II** exhibit similar features (Figure S1). The hexameric $[Ge_6(\mu_2\text{-}OH)_6(C_2H_4O_7P_2)_6]^{6-}$ moiety gives the following resonances for **I** and **II**, respectively: quaternary carbon atoms (C1, C3, C5) 70.9 and 71.3 ppm; methyl (C2, C4, C6) carbon atoms 18.6 and 19.9 ppm. This moiety has three crystallographically inequivalent quaternary and methyl carbon atoms, but three resonances are only clearly observed (as shoulders) in the quaternary carbon region of **I**. Above 100 ppm, resonances are assigned to the aromatic carbon atoms involved in the extensive columnar π–π stacking.

^{1}H Spectra: Hydrogen-Bonding Assignment

The F1 projection of the ^{1}H-^{1}H FS-LG and the ^{1}H fast (30 kHz) MAS spectra (Figure 6) have similar resolution, and show up to 8 resolved peaks. However, a judicious choice of 2D F2 slices proves the presence of some 10 resonances (consider Figure 6c). The resonances (H^a-H^c) in the range 16.6–13.1 ppm are assigned to strong hydrogen bonds, because of their relatively high-frequency shifts (Table 2). Hydrogen-bonded systems involving carboxylic (C=O) and phosphonic (P=O) acids as electron donors (i.e. proton acceptors) were reported to resonate in the ranges 12–20 ppm and 11–17 ppm, respectively.[43] In **I**, the P=O groups are within the hydrogen-bonding distance of the OH groups of the 8-hydroxyquinoline (ArO–H) moieties ($r_{O\cdots O}$ = 2.61 Å). P=O groups involved in hydrogen bonds with OH residues have been reported to resonate at 11–12 ppm.[20,43] Resonance H^c is tentatively attributed to ArO–H···O=P environments. Such hydrogen bonds (ArO–H···O=P) are likely to be stronger than other CO–H···O=P bonds[20] because the conjugated base (ArO^-) of the hydrogen donor (ArO–H) is weak, owing to aromatic ring stabilisation. When the acidity of a hydrogen-bonded OH group increases, its chemical shift also increases, and the resonance H^c therefore appears at a chemical shift larger than 12 ppm.

The crystallographic N···O distance range (2.72–2.78 Å) suggests that the protonated nitrogen atom of 8-hydroxyquinoline is hydrogen-bonded to water molecules (N^+–H···OH_2). The presence of N^+–H groups involved in this type of interaction is likely because the charge of the anionic hexameric unit must be compensated by H^+. Protonation and hydrogen bonding result in a significant increase in the ^{1}H chemical shift. Thus, the H^a and H^b resonances

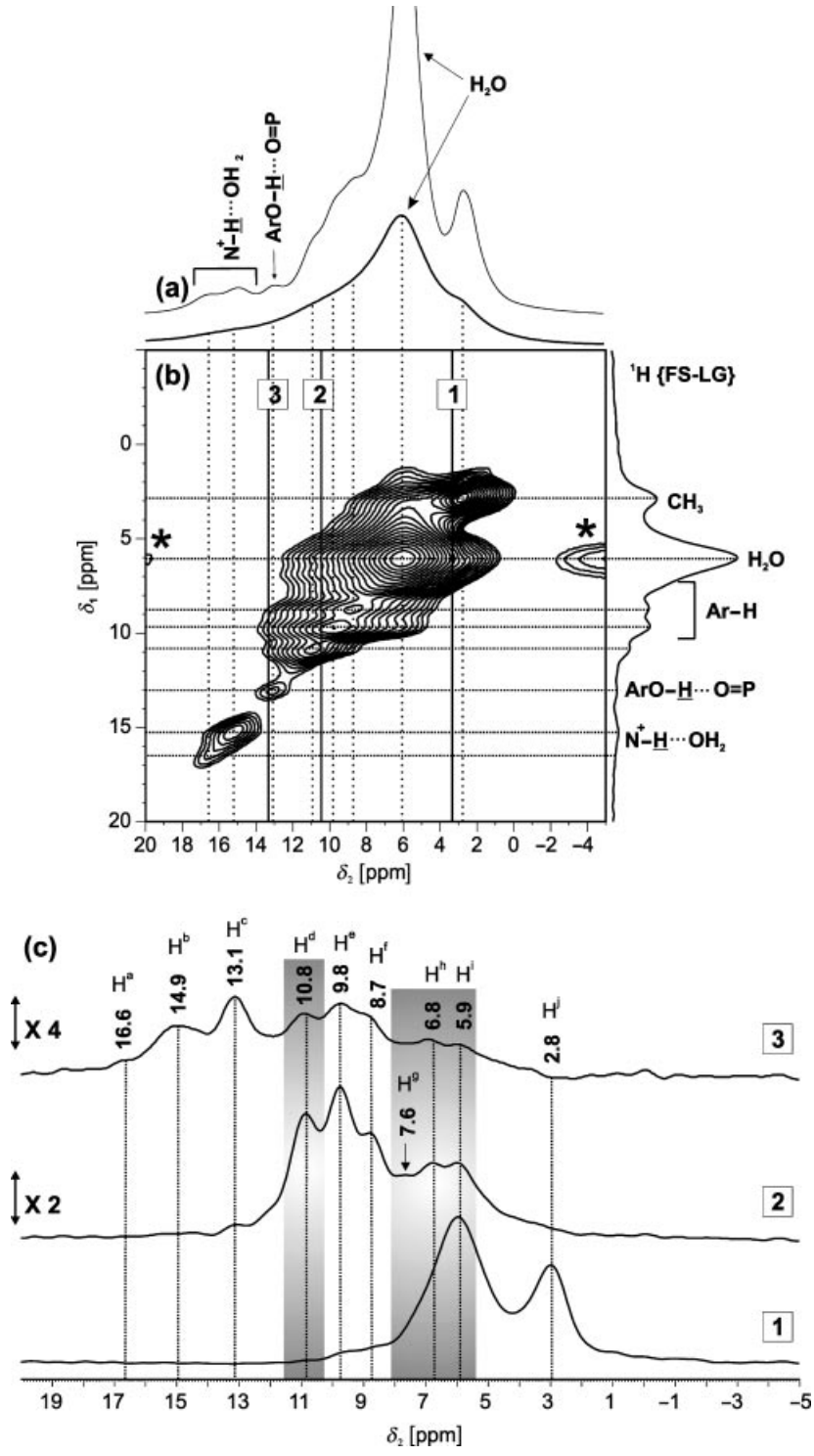

Figure 6. (a) ^{1}H MAS and (b) 2D ^{1}H-^{1}H FS-LG spectra of **I**. (c) F2 cross-sections of the ^{1}H-^{1}H FS-LG spectrum of **I** taken at 3.4, 10.5 and 13.3 ppm. Asterisks depict spinning sidebands.

at δ = 16.6 and 14.9 ppm are tentatively assigned to N^+–H···OH_2 environments (and confirmed below by ^{1}H-^{1}H DQF spectroscopy).

The ^{1}H resonances H^i and H^j at ca. 5.9 and 2.8 ppm, respectively, are assigned to lattice water and CH_3 groups. The remaining ^{1}H peaks between ca. 6 and 11 ppm cannot be assigned without information from other 2D techniques (see below).

The ^{1}H-^{1}H FS-LG spectrum of **II** (Figure S8) displays fewer resonances than that of **I**. In particular, a peak is observed at ca. 15.1 ppm, which shows the presence of strong hydrogen bonds between the protonated nitrogen

Table 2. ^1H chemical shift assignment of **I**.

^1H[a]	SQ δ_H [ppm]	DQ δ_H [ppm]	DQ coherences[b]
ArN^+–*H* (H^a)	16.6	26.4	$H^a\cdots H^e$
ArN^+–*H* (H^b)	14.9	24.7	$H^b\cdots H^e$
		22.5	$H^b\cdots H^g$
ArO–*H* (H^c)	13.1	20.7	$H^c\cdots H^g$
CO–*H* (H^d)	10.8	19.5	$H^d\cdots H^f$
		17.6	$H^d\cdots H^h$
		13.6	$H^d\cdots H^j$
Ar–*H* (H^e)[c]	9.8	26.4	$H^e\cdots H^a$
		24.7	$H^e\cdots H^b$
Ar–*H* (H^f)	8.7	16.3	$H^f\cdots H^g$
		11.5	$H^f\cdots H^j$
		19.5	$H^f\cdots H^d$
Ar–*H* (H^g)[c]	7.6	16.3	$H^g\cdots H^f$
		20.7	$H^g\cdots H^c$
		22.5	$H^g\cdots H^b$
HO–*H* (H^h, H^i)[d]	6.8, 5.9	8.7	$H^i\cdots H^j$
		17.6	$H^h\cdots H^d$
CH_3 (H^j)	2.8	13.6	$H^j\cdots H^d$
		11.5	$H^j\cdots H^f$

[a] Resonances observed in the ^1H-^1H FS-LG and ^1H-^1H DQF spectra are considered. [b] DQ coherences are not considered for the self-correlation peaks (diagonal peaks). [c] There is evidence of $H^e\cdots H^j$ and $H^g\cdots H^j$ correlations, but their observation is difficult (Figure 7b). [d] These ^1H resonances refer to the two resolved peaks (H^h and H^i) observed in Figure 6, which are tentatively assigned to H_2O protons.

[N(21)] of 1,10-phenanthroline and the P=O(6) groups of the anionic unit ($r_{N(21)\cdots O(14)}$ = 2.68 Å, Table S6). This supports the assignment of resonances H^a and H^b proposed above for compound **I**.

The presence of signals in the ^1H-^1H DQF spectrum (Figure 7b) reveals dipolar couplings between nuclei and allows the identification of mobile water molecules by comparison with the 30 kHz MAS ^1H NMR spectrum (Figure 7a). The latter is dominated by mobile water molecules located in the channels, which resonate at ca. 5.9 and 6.8 ppm for **I** and **II**, respectively (Figure 7a and S9a). This peak is suppressed in DQF experiments, simplifying the spectra (Figure 7b and S9b). In the following discussion, SQ coherences (Table 2) identified from ^1H-^1H FS-LG are taken into consideration in the study of the SQ-DQ correlations.

The Ar-H protons (H^e, H^f and H^g, Scheme 1) are classed into three main groups on the basis of the chemical shifts of their resonances, which are expected in the order $\delta(H^e) > \delta(H^f) > \delta(H^g)$. In solution, pure 8-hydroxyquinoline resonates in the range 7.3–9.0 ppm, while for **I**, the chemical shifts range from 7.6 and 9.8 ppm. The identification of the Ar-H resonances was made possible by analysing the DQ frequency of the off-diagonal peaks (Figure 7b) that involve the hydrogen-bonded ^1H resonances (H^a, H^b and H^c), which are well resolved.

In the 2D ^1H-^1H DQF spectrum, H^e resonances exhibit strong off-diagonal correlations with those of H^a and H^b as these protons are in *ortho* positions (adjacent) and are thus relatively close (2.16–2.28 Å). DQ chemical shifts of ca. 26.4 (16.6 + 9.8) and 24.7 (14.9 + 9.8) ppm for H^a and H^b, respectively, are observed. This evidence allows the assignment of

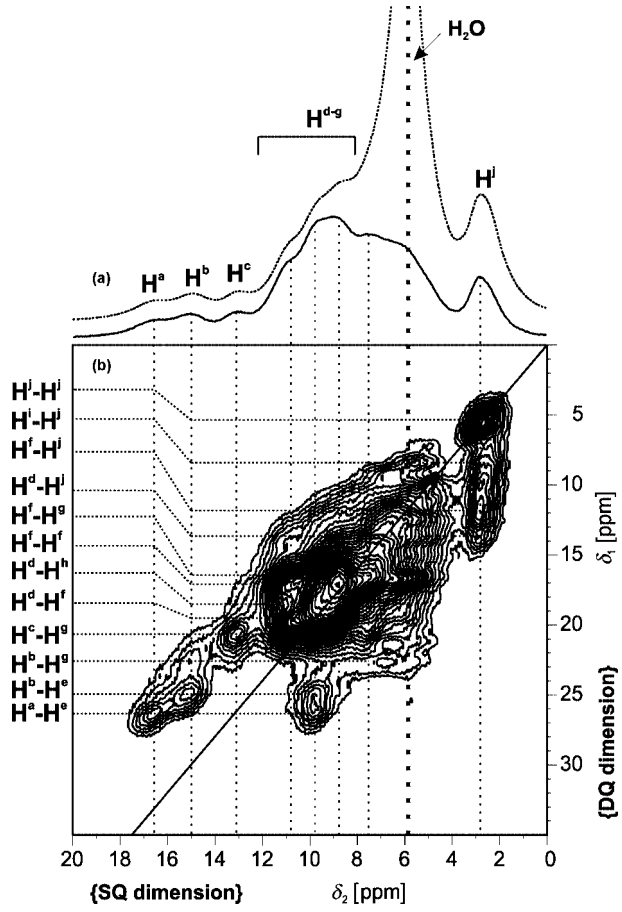

Figure 7. (a) ^1H MAS and (b) ^1H-^1H DQF MAS NMR spectra of **I**.

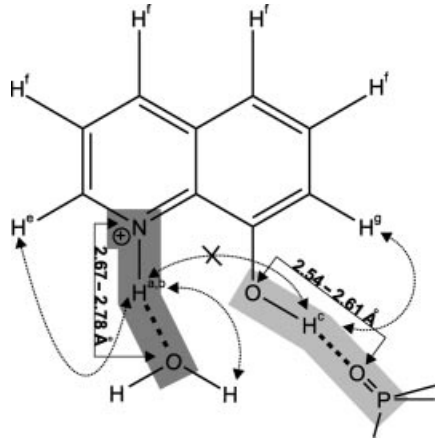

Scheme 1. Hydrogen bonds formed by 8-hydroxyquinoline in compound **I**. Dashed arrows show the interactions revealed by XRD (Table S5).

H^a and H^b to N^+–H···OH_2 bonds determined by XRD. In a similar way, the resonance at ca. 13.1 ppm (H^c) has a DQ frequency of ca. 20.7 ppm, which allows for the assignment of the peak at ca. 7.6 ppm to H^g, as this proton is also in an *ortho* position to H^c. Besides, H^c is not correlated with H^e because no DQ frequency appears at ca. 22.9 (13.1 + 9.8) ppm. Therefore, H^c is not assigned to N^+–H protons in-

volved in hydrogen bonds with water; these latter protons (H^a and H^b) have always shown to be correlated with H^e (Scheme 1).

Because the peaks are hidden by neighbouring resonances, the correlations involving H^f are harder to ascertain. The remaining peak in the aromatic region at 8.7 ppm is assigned to H^f. This is supported by the DQ self-correlation $H^f\cdots H^f$ peak at ca. 17.4 ppm in the DQ dimension. The assignment of DQ coherences involving $H^f\cdots H^g$ and $H^f\cdots H^e$ was not possible because of the lack of resolution.

We now consider the tentative assignment of the resonances of **I** at ca. 10.8 (H^d) and 6.8 ppm (H^h). The 2D ^{1}H-^{1}H DQF spectrum suggests that these protons are close in space and lead to a DQ frequency of ca. 17.6 ppm ($H^d\cdots H^h$). In accord, XRD data reveals the presence of hydrogen bonds involving the H^d protons of tertiary alcohol groups of $HEDP^{4-}$ and the H^h protons of water molecules. Additionally, the H^d protons (δ =10.8 ppm) exhibit another DQ frequency at 13.6 (10.8 + 2.8) ppm, showing the close proximity (<0.35 nm) between the CO–H and CH_3 groups. The spectrum also provides evidence for the proximity between the CH_3 protons (H^j) and 8-hydroxyquinoline because correlations with all the Ar-H (H^e, H^f and H^g) resonances (Table 2 and Figure 3b) are observed.

As far as compound **II** is concerned, the main conclusion is that the high-frequency resonance (at δ = 15.1 ppm) may be assigned to N^+–H···O=P hydrogen bonds (Figure S9b). Indeed, **II** possesses only a single type of very short (1.86 Å) hydrogen bond.

The ^{1}H-^{1}H exchange RFDR (Figure 8) and ^{1}H-^{1}H DQF experiments provide complementary information — the former maps correlations involving both mobile and rigid species, while the latter maps only those involving the rigid species.

In **I**, the lattice water resonances (H^i) are correlated with all peaks even at low mixing times, revealing the presence of water molecules dispersed throughout the structure. On the other hand, at a mixing time of 0.53 ms (Figure 8a), the CH_3 (H^j) protons are not correlated with H^a, H^b and H^c, thus supporting the DQF results and confirming that the H^e protons are only near H^a and H^b (hydrogen bonds involving N–H^+–OH_2). Moreover, a clear correlation between H^c and H^g is observed. This pair of resonances ($H^c\cdots H^g$) is strongly correlated at low mixing times (Figure 8a), supporting the information given by ^{1}H-^{1}H DQF spectroscopy (Figure 7b). The ^{1}H-^{1}H RFDR spectrum of structure **II** is far less informative and will not be further discussed (Figure S10).

The ^{1}H-^{1}H DQF spectrum of **I** also reveals important information on the spatial arrangement of the organic residues. Excellent reviews are available on the study of three-dimensional crystal packing based on ring-current effects arising from the aromatic π orbitals.[21,44,45] Moreover, the influence of ring currents on neighbouring molecules shifts the chemical shifts over a range of 2–5 ppm.[46] The Ar-H resonances (H^e, H^f and H^g) of **I** are shifted to high frequency relative to the resonances of 8-hydroxyquinoline in solution, which may be due to either amine protonation or

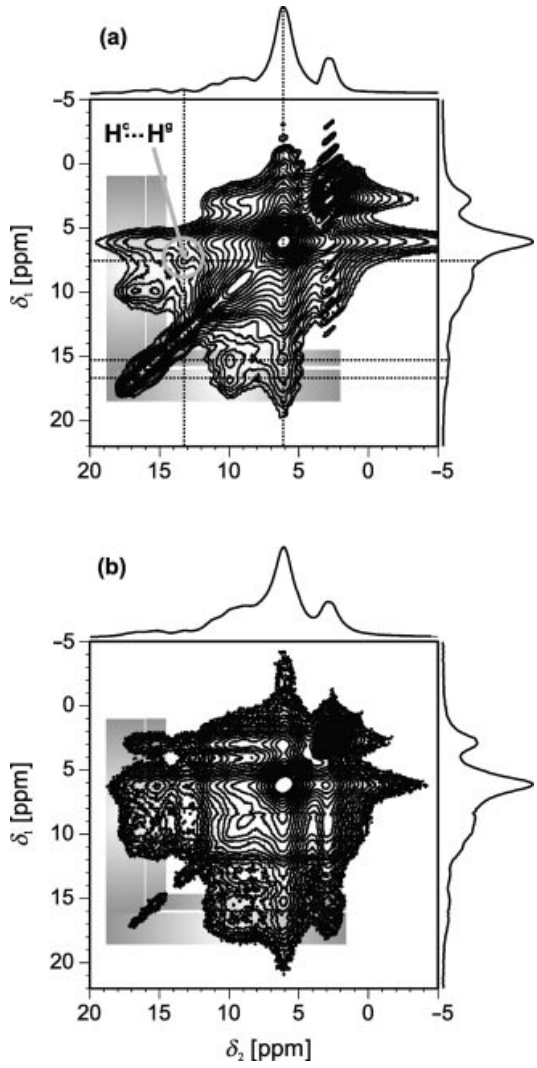

Figure 8. 2D ^{1}H-^{1}H exchange RFDR spectra recorded with mixing times of (a) 0.53 ms and (b) 3.2 ms.

small ring-current effects caused by adjacent molecules. The relative orientation of adjacent 8-hydroxyquinoline molecules may be studied on the basis of the ^{1}H-^{1}H DQF spectrum. The H^b resonance shows an additional off-diagonal correlation at a DQ frequency of 22.5 ppm, clear evidence of spatial proximity between protons H^b and H^g. Because the intra- and intermolecular distances between these protons are 5.3 and 3.2 Å, respectively, the SQ-DQ correlation is ascribed to the latter proton resonances. Moreover, the absence of diagonal peaks involving the resolved hydrogen bonds indicates that H^a, H^b and H^c are protons belonging to separate molecules (Figure 7b).

The ^{1}H projection of the ^{1}H-^{31}P FS-LG spectra of **I** (Figure S11) is better resolved than the F1 projection of the ^{1}H-^{1}H FS-LG spectra (Figure 6b). Alternatively, the ^{1}H-^{31}P FS-LG spectra are useful to probe the hydrogen bonds between the $HEDP^{4-}$ phosphonate group and the 8-hydroxyquinoline aromatic residues. At short contact times (0.2 ms), the ^{1}H-^{31}P FS-LG H^c resonances are slightly more

intense than those for H^a and H^b, which indicates that the H^c protons are hydrogen bonded to P=O groups, as mentioned above (Scheme 1).

Photoluminescence Spectroscopy

Figure 9 shows the excitation spectrum of **I** recorded at 14 K. The spectrum consists of a broad band between 270 and 440 nm, assigned to aromatic ring π–π* transitions.[47] The excitation of **I** within such states leads to the observation of both a main band in the range 440 to 650 nm, peaking at 530 nm, and an emission component at higher wavelengths (Figure 9a). According to the crystal structures, the aromatic moieties have two distinct packing environments: columnar π···π stacking and adjacent molecules connected to the columns through weak C–H···π interactions. Hence, the former band may be assigned to the π–π* 0-phonon transition of the hydroquinoline adjacent rings,[47] which corresponds to a triplet-state energy of 18900 cm^{-1}, while the band at higher wavelengths is attributed to excimer formation through π···π hydroquinoline interactions. At room-temperature, no efficient emission could be detected, which indicates the presence of thermally activated non-radiative channels in **I**.

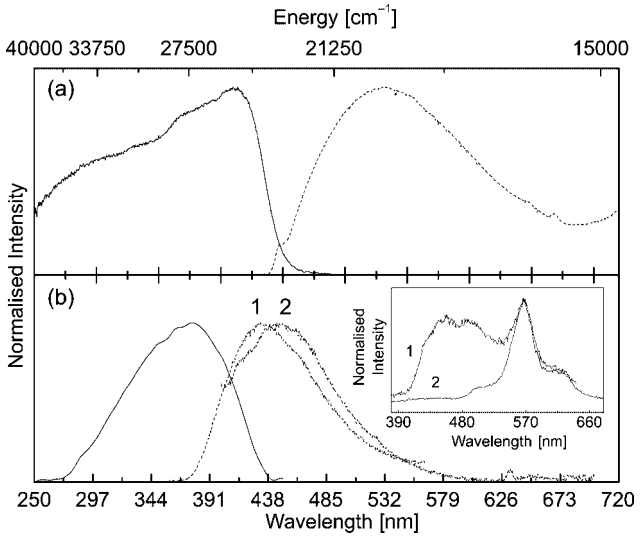

Figure 9. Excitation (solid line) and emission (dashed line) spectra of the complexes of (a) **I** and (b) **II** recorded at 14 K and room temperature, respectively. The excitation and emission spectra of **I** were monitored at 535 nm and excited at 408 nm, whereas for **II**, the monitoring wavelength was 490 nm and the excitation wavelengths were 330 nm (1) and 365 nm (2). The inset shows the time-resolved emission spectrum (14 K) of **II**, acquired with a starting delay of 0.05 ms and an acquisition window of 10.00 ms.

Figure 9b shows the room-temperature excitation spectra of **II** monitored at 490 nm. The spectrum displays a large broad band between 270 and 400 nm, peaking at 367 nm, ascribed to aromatic ring π–π* transitions.[48] The room-temperature reflectance spectrum (not shown) resembles the excitation spectra, displaying an absorption edge at 370 nm. This value is shifted to the red when compared with the singlet energy of the neutral 1,10-phenanthroline ligand (320 nm, 31250 cm^{-1}).[49] This energy difference is induced by the different local environment of 1,10-phenanthroline, in particular, the metal coordination and the packing of the complex in **II**.

Under UV excitation (Figure 9b), the emission of **II** consists of a large asymmetrical band between 380 and 550 nm. For excitation wavelengths in the range 270–370 nm, the emission energy peaks at 430 nm and does not depend on the excitation wavelength. For higher excitation wavelengths, a broadening and red-shift of the emission spectra are observed. The dependence on the excitation wavelength and the asymmetric shape of the emission suggest the appearance of a new emitting species, preferentially excited at higher wavelengths. As suggested for **I**, the presence of two distinct emission components may be due to the presence of two different packing environments for the 1,10-phenanthroline rings. The spectra acquired for excitation wavelengths between 270–370 nm may correspond to the preferential emission arising from the adjacent 1,10-phenanthroline rings. Like the excitation spectrum (Figure 9a), their emission energy is shifted with respect to that of the free 1,10-phenanthroline chromophore, whose lowest triplet-state energy (π–π* 0-phonon transition) peaks at 366 nm (27322 cm^{-1});[50,51] however, the emission energy is very similar to that observed for $Gd(phen)_2Cl_3\cdot 2H_2O$[50], with a lowest triplet-state energy of 453 nm (22075 cm^{-1}).[52] The emission component at lower energy may be ascribed to the formation of an excimer through π···π phenanthroline interactions, as observed in 1,10-phenanthroline compounds with the same crystal packing of **II**.[50,51]

The presence of two distinct emissions in **II** was further established and investigated by time-resolved emission and lifetime measurements. These studies were performed at 14 K, since the room-temperature time-scale for the photoluminescence mechanisms is smaller than the detection limit of our equipment (10^{-5} s). For lower excitation wavelengths, the spectrum consists of a structured broad band (inset in Figure 9b). Increasing the excitation wavelength results in a decrease in the relative intensity of the lower-wavelength-side of the spectra, which further indicates the presence of two distinct emitting species. Such an intensity decrease suggests that the time scale for the emission mechanisms of the emission component at lower wavelengths is smaller than that of the lower-wavelength emission. The short-lived emission is consistent with a monomer component, whereas the longer-lived and lower-energy emission is compatible with the formation of an excimer.[50,51,53] The excimer emission decay curve was monitored at 568 nm under 330 nm excitation wavelength (not shown). The decay curve is well reproduced by a single exponential function, which yields a lifetime of 4.33 ± 0.11 ms.

Conclusions

Two germanium-$hedp^{4-}$ solids with heteroaromatic amines, 8-hydroxyquinoline (in **I**) and 1,10-phenanthroline (in **II**), have been prepared and characterised by single-crys-

tal XRD, thermogravimetry and FTIR and UV/Vis spectroscopy. High-resolution solid-state NMR spectroscopy has been used to study the complex hydrogen-bonded networks, particularly in compound **I**. Certain details of the crystal structure of **I** have been elucidated, mainly those involving the occurrence of π–π stacking of 8-hydroxyquinoline and the relative orientation of adjacent such molecules. It has been shown that the combination of homonuclear recoupling techniques (2D ^{1}H-^{1}H DQF, 2D ^{1}H-^{1}H RFDR MAS NMR) and CRAMPS techniques (2D ^{1}H-^{1}H FS-LG, ^{1}H-^{31}P FS-LG) provides a powerful toolbox for the characterisation of organic–inorganic hybrid materials.

Compound **II** displays an emission from the lowest triplet-state energy (π–π* 0-phonon transition) of the aromatic rings, which peaks at ca. 320 nm (31250 cm^{-1}) in the range 14 K to room temperature, whereas the triplet emission of complex **I** at ca. 530 nm (18868 cm^{-1}) is detected at low temperature. A long-lived and low-energy emission component, resulting from the formation of an excimer state and originating from π···π stacking of 1,10-phenanthroline and hydroxyquinoline residues, was observed for **I** and **II**, respectively.

Experimental Section

General: Chemicals were readily available from commercial sources and were used as received without further purification. Elemental analyses for carbon, hydrogen and nitrogen were performed on a CHNS-932 Elemental Analyser instrument at the University of Aveiro. FTIR spectra were measured by using KBr disks (Aldrich, 99%, FTIR grade) on a Matson 7000 FTIR spectrometer. FT-Raman spectra were measured on a Bruker RFS 100 with a Nd:YAG coherent laser (λ = 1064 nm). Thermogravimetric analyses (TGA) were carried out by using a Shimadzu TGA-50 instrument and Differential Scanning Calorimetry (DSC) analyses on a Shimadzu DSC-50 instrument with a heating rate of 5 °C/min under a nitrogen atmosphere with flow rate of 20 cm^3/min. PL and time-resolved spectra were recorded between 14 K and room temperature with a TRIAX 320 emission monochromator (Fluorolog-3, Jobin Yvon-Spex) coupled to an R928 Hamamatsu photomultiplier, using the front face acquisition mode.

Synthesis of (Hhqn)$_6$[Ge$_6$(OH)$_6$(hedp)$_6$]·2(hqn)·33H$_2$O (I): A suspension of 1-hydroxyethylidenediphosphonic acid (0.200 g, H_4hedp, $C_2H_8O_7P_2$, ≥97%, Fluka), germanium(IV) oxide amorphous (0.100 g, GeO_2, 99.99%, Aldrich), and 8-hydroxyquinoline (0.140 g, hqn, C_9H_7NO, 99%, Merck) in distilled water (ca. 12 g) was stirred thoroughly for 30 min at ambient temperature. The reactive mixture was transferred to a PTFE-lined stainless steel reaction vessel (ca. 40 cm^3), which was then placed inside an oven. The temperature was gradually increased to 120 °C and kept constant for 3 d, after which the vessel was cooled slowly to ambient temperature before opening. The resulting light-yellow phase was washed with distilled water, filtered and air dried at ambient temperature. The single-crystalline phase decomposes into a microcrystalline powder during this drying stage. Hence, (Hhqn)$_6$[Ge$_6$(OH)$_6$(hedp)$_6$]·2(hqn)·33H$_2$O samples suitable for single-crystal X-ray diffraction measurements were isolated while still wet directly from the autoclave mother liquor by slow evaporation at ambient temperature for 2 d. Elemental composition (based on single-crystal data for $C_{84}H_{158}Ge_6N_8O_{89}P_{12}$, M_W 3511.36): calcd. C 28.73, N 3.20, H 4.54%; found C 28.87, N 3.08, H 4.51%. TGA data (mass losses): 20–86 °C: 14.2%; 86–155 °C: 3.3%; 155–210 °C: 2.3%; 210–400 °C: 5.5%. DSC peaks (endothermic processes): 76, 103, 184, 258 and 336 °C. Selected IR (KBr pellet) and Raman (in italics inside the parenthesis, cm^{-1}) data: ν(HO–H/GeO–H/CO–H, with evidence of H-bonding) = 3430 vs/br., 3254 vs/br., 3093 vs/br. (*3116 w*); ν(aromatic NH$^+$) = 2790 m/br.; ν(C–H, aromatic) = 3093 br. (*3069 m*); ν_{as}(C–H in –CH$_3$) = 2969 br. (*2979 w*, *2937 w*); ν_s(C–H in –CH$_3$) = (*2875 w*); δ_s(CO–H) and δ_{as}(CH$_3$) = 1421 m, 1404 m; δ_s(CH$_3$) = 1384 m (*1385 s*); ν(N$^+$–H) = 2580 br.; δ(–NH$^+$) = 1559 m; ν(P=O) and ν(C–O) = 1187 s and 1169 s (*1314*); ν(C–C, skeletal vibrations) = 1603 m (*1606 m*); δ(O–H, lattice water) = 1635 m (*1634 w*); ν(C–N, heteroaromatic amines) and δ(O–H, aromatic) = 1312 m (*1308 w*, *1279 w*); ν(P–O) = 1010 vs (*1064 m*, *1038 w*); γ(C–C) = 488 w (*542 w*, *490 m*, *474 m*, *410 m*), various modes; γ(O–H, under H-bonding) = 976 br./vs; γ(C–H, aromatic) = 824 m (*716* vs); ω(O–H, under H-bonding) = 583 br./m (*578*) cm^{-1}.

Synthesis of (Hphen)$_6$[Ge$_6$(OH)$_6$(hedp)$_6$]·2(phen)·20H$_2$O (II): A suspension of 1-hydroxyethylidenediphosphonic acid (0.200 g, H_4hedp, $C_2H_8O_7P_2$, ≥97%, Fluka), amorphous germanium(IV) oxide (0.240 g, GeO_2, 99.99%, Aldrich) and 1,10-phenanthroline monohydrate (0.190 g, phen, $C_{12}H_8N_2$·H_2O, ≥99.0%, Fluka) in distilled water (ca. 16 g) was stirred thoroughly for 30 min at ambient temperature. The reactive mixture was transferred to a PTFE-lined stainless steel reaction vessel (ca. 40 cm^3), which was then placed inside an oven. The temperature was gradually increased to 120 °C and kept constant for 3 d, after which the vessel was cooled slowly to ambient temperature before opening. The isolated microcrystalline light-brown phase was washed with distilled water, filtered and air-dried at ambient temperature. Single crystals of (Hphen)$_6$[Ge$_6$(OH)$_6$(hedp)$_6$]·2(phen)·20H$_2$O suitable for X-ray diffraction measurements were harvested from the autoclave mother liquor by slow evaporation at ambient temperature over 1 d. Elemental composition (based on single-crystal data for $C_{108}H_{140}Ge_6N_{16}O_{68}P_{12}$, M_W 3557.54): calcd. C 36.46, N 6.33, H 3.97%; found C 35.47, N 5.46, H 4.20. TGA data (mass losses): 20–125 °C: 10.3%; 125–364 °C: 10.0%. Selected IR (KBr pellet) and Raman (in italics inside the parenthesis, cm^{-1}) data: ν(HO–H/GeO–H/CO–H, with evidence of H-bonding) = 3389 vs/br., 3237 vs/br.; ν(aromatic NH$^+$) = 2532 s/br.; ν(C–H, aromatic) = 3062 m (*3066 m*); ν_{as}(C–H in –CH$_3$) = 2932 m (*2990 w*, *2933 w*); ν_s(C–H in –CH$_3$) = 2807 s, 2879 s (*2872 w*); δ_{as}(CH$_3$) = 1452 m, 1469 m (*1452 s*, *1415* vs); δ_s(CH$_3$) = 1373 w (*1373 m*); ν(C–N, heteroaromatic amines) = 1316 m (*1316 w*); δ(CO–H) = 1289 w (*1286 w*); ν(N$^+$–H) = 2532 br.; δ(–NH$^+$) = 1542 s; δ(O–H, lattice water) = 1632 s/br. (*1629 w*); ν(C–C, skeletal vibrations) = 1617 s, 1596 s (*1615 m*, *1596 m*); ν(P=O) and ν(C–O) = 1185 vs/br. (*1189 w*); ν(P–O) = 1053 s (*1045 m*); γ(C–C) = 487 s, 461 s (*550 w*, *508 w*, *461 w*), various modes; γ(O–H, under H-bonding) = 971 vs/br., various modes; γ(C–H, aromatic) = 847 vs, 816 s (*848 w*); ω(O–H, under H-bonding) = 620 vs, 592 vs, 568 vs, various modes (*598 w*) cm^{-1}.

CCDC-614629 and CCDC-614630 for **I** and **II** contain the supplementary crystallographic data for this paper. These data can be obtained free of charge from The Cambridge Crystallographic Data Centre via www.ccdc.cam.ac.uk/data_request/cif.

Supporting Information (see footnote on the first page of this article): Thermoanalytical and infrared results and detailed discussion are included. Technical and experimental details on the single-crystal X-ray diffraction, solid-state NMR spectroscopy and photoluminescence studies are also included. Additional structural drawings emphasizing the [Ge$_6$(μ_2-OH)$_6$($C_2H_4O_7P_2$)$_6$]$^{6-}$ moiety (and tables containing crystallographic bond lengths and angles), the or-

ganic frameworks and the solvent-accessible cavities are given. Results of a Cambridge Structural Database Survey for typical Ge–O–Ge bonds are presented. Tables summarising hydrogen-bonding geometries for the two compounds and additional NMR spectra [$^{13}C\{^1H\}$ RAMP-CP, ^1H-^1H FS-LG, ^1H MAS (for **II**), 2D ^1H-^1H RFDR (for **II**), ^1H-^{31}P FS-LG] are also included.

Acknowledgments

We are grateful to FEDER, POCTI (Portugal) and to the Portuguese Foundation for Science and Technology (FCT) for their financial support and also to the Ph.D. and postdoctoral research grants Nos. SFRH/BD/13858/2003 (to L. M.) and SFRH/BPD/9309/2002 (to F.-N. S.), respectively.

[1] A. Clearfield, *Progress in Inorganic Chemistry Vol. 47* (Ed.: K. D. Karlin), New York, **1998**.
[2] G. Férey, *Chem. Mater.* **2001**, *13*, 3084.
[3] D. Hagrman, P. J. Hagrman, J. Zubieta, *Angew. Chem. Int. Ed.* **1999**, *38*, 3165.
[4] P. J. Hagrman, R. C. Finn, J. Zubieta, *Solid State Sci.* **2001**, *3*, 745.
[5] B. Moulton, M. J. Zaworotko, *Chem. Rev.* **2001**, *101*, 1629.
[6] J. L. C. Rowsell, O. M. Yaghi, *Angew. Chem. Int. Ed.* **2005**, *44*, 4670.
[7] C. Sanchez, G. J. D. A. A. Soler-Illia, F. Ribot, T. Lalot, C. R. Mayer, V. Cabuil, *Chem. Mater.* **2001**, *13*, 3061.
[8] E. W. Stein Sr, A. Clearfield, M. A. Subramanian, *Solid State Ionics* **1996**, *83*, 113.
[9] P. Ayyappan, O. R. Evans, B. M. Foxman, K. A. Wheeler, T. H. Warren, W. Lin, *Inorg. Chem.* **2001**, *40*, 5954.
[10] M. Eddaoudi, D. B. Moler, H. Li, B. Chen, T. M. Reineke, M. O'Keeffe, O. M. Yaghi, *Acc. Chem. Res.* **2001**, *34*, 319.
[11] M. Eddaoudi, O. M. Yaghi, H. Li, *J. Am. Chem. Soc.* **2000**, *122*, 1391.
[12] R. Murugavel, M. G. Walawalkar, M. Dan, C. N. R. Rao, H. W. Roesky, *Acc. Chem. Res.* **2004**, *37*, 763.
[13] B. Zhang, D. M. Poojary, A. Clearfield, *Inorg. Chem.* **1998**, *37*, 249.
[14] M. P. Jensen, J. V. Beitz, R. D. Rogers, K. L. Nash, *J. Chem. Soc., Dalton Trans.* **2000**, 3058–3064.
[15] D. M. Poojary, B. Zhang, A. Clearfield, *Angew. Chem. Int. Ed. Engl.* **1994**, *33*, 2324.
[16] E. N. Rizkalla, *Rev. Inorg. Chem.* **1983**, *5*, 233.
[17] J. Simon, D. A. Wilson, J. R. Garlich, D. E. Troutner (Dow Chemical Company), patent no. 899734, **1989**.
[18] K. L. Nash, J. Ferraro, R. D. Rogers, J. Zhang, *Inorg. Chim. Acta* **1998**, *269*, 211.
[19] A. E. Aliev, K. D. M. Harris, *Probing Hydrogen Bonding in Solids using Solid State NMR Spectroscopy*, Springer-Verlag Berlin, Berlin, **2004**.
[20] S. Pawsey, M. McCormick, S. De Paul, R. Graf, Y. S. Lee, L. Reven, H. W. Spiess, *J. Am. Chem. Soc.* **2003**, *125*, 4174–4184.
[21] I. Schnell, *Prog. Nucl. Magn. Reson. Spectrosc.* **2004**, *45*, 145–207.
[22] E. Brunner, U. Sternberg, *Prog. Nucl. Magn. Reson. Spectrosc.* **1998**, *32*, 21–57.
[23] G. R. Goward, M. F. H. Schuster, D. Sebastiani, I. Schnell, H. W. Spiess, *J. Phys. Chem. B* **2002**, *106*, 9322–9334.
[24] I. Schnell, S. P. Brown, H. Y. Low, H. Ishida, H. W. Spiess, *J. Am. Chem. Soc.* **1998**, *120*, 11784–11795.
[25] S. P. Brown, I. Schnell, J. D. Brand, K. Mullen, H. W. Spiess, *Phys. Chem. Chem. Phys.* **2000**, *2*, 1735–1745.
[26] I. Schnell, H. W. Spiess, *J. Magn. Reson.* **2001**, *151*, 153–227.
[27] L. Mafra, F. A. A. Paz, F. N. Shi, J. Rocha, T. Trindade, C. Fernandez, A. Makal, K. Wosniak, J. Klinowski, *Chem. Eur. J.* **2006**, *12*, 363–375.
[28] D. Massiot, B. Alonso, F. Fayon, F. Fredoueil, B. Bujoli, *Solid State Sci.* **2001**, *3*, 11–16.
[29] L. Mafra, J. Rocha, C. Fernandez, F. A. A. Paz, *J. Magn. Reson.* **2006**, *180*, 236–244.
[30] M. Feike, D. E. Demco, R. Graf, J. Gottwald, S. Hafner, H. W. Spiess, *J. Magn. Reson. Ser. A* **1996**, *122*, 214–221.
[31] I. Schnell, A. Watts, H. W. Spiess, *J. Magn. Reson.* **2001**, *149*, 90–102.
[32] A. E. Bennett, C. M. Rienstra, J. M. Griffiths, W. Zhen, P. T. Lansbury Jr, R. G. Griffin, *J. Chem. Phys.* **1998**, *108*, 9463–9479.
[33] A. E. Bennett, J. H. Ok, R. G. Griffin, S. Vega, *J. Chem. Phys.* **1992**, *96*, 8624–8627.
[34] A. Bielecki, A. C. Kolbert, M. H. Levitt, *Chem. Phys. Lett.* **1989**, *155*, 341–346.
[35] I. I. Seifullina, E. E. Martsinko, G. G. Aleksandrov, V. S. Sergienko, *Russ. J. Inorg. Chem.* **2004**, *49*, 844–852.
[36] S. Nishigaki, H. Yoshioka, K. Nakatsu, *Acta Crystallogr., Sect. B* **1978**, *34*, 875–879.
[37] F. A. A. Paz, J. Klinowski, *J. Phys. Org. Chem.* **2003**, *16*, 772–782.
[38] P. van der Sluis, A. L. Spek, *Acta Crysallogr., Sect. A* **1990**, *46*, 194–201.
[39] A. L. Spek, *J. Appl. Crystallogr.* **2003**, *36*, 7–13.
[40] A. L. Spek, *Acta Crystallogr., Sect. A* **1990**, *46*, C34.
[41] Y. Ohashi, K. Yanagi, T. Kurihara, Y. Sasada, Y. Ohgo, *J. Am. Chem. Soc.* **1981**, *103*, 5805–5812.
[42] *Cerius^2, Version, 4.2*, *Molecular Simulations Inc.*, San Diego, **2000**.
[43] R. K. Harris, P. Jackson, L. H. Merwin, B. J. Say, *J. Chem. Soc., Faraday Trans. 1* **1988**, *84*, 3649–3672.
[44] M. Umetsu, J. G. Hollander, J. Matysik, Z. Y. Wang, T. Adschiri, T. Nozawa, H. J. M. Groot, *J. Phys. Chem. B* **2004**, *108*, 2726–2734.
[45] J. S. Waugh, R. W. Fessenden, *J. Am. Chem. Soc.* **1957**, *79*, 846–849.
[46] A. Hoffmann, D. Sebastiani, E. Sugiono, S. Yun, K. S. Kim, H. W. Spiess, I. Schnell, *Chem. Phys. Lett.* **2004**, *388*, 164–169.
[47] D. Imbert, S. Comby, A.-S. Chauvin, J.-C. G. Bünzli, *Chem. Commun.* **2005**, 1432–1434.
[48] C.-J. Xua, F. Xiea, X.-Z. Guoa, H. Yang, *Spectrochim. Acta* **2005**, *61*, 2005–2008.
[49] H. Xin, M. Shi, X. C. Gao, Y. Y. Huang, Z. L. Gong, D. B. Nie, H. Cao, Z. Q. Bian, F. Y. Li, C. H. Huang, *J. Phys. Chem. B* **2004**, *108*, 10796–10800.
[50] R. Caballo, B. Covelo, C. Lodeiro, E. M. Vazquez-López, *CrystEngCommun* **2005**, *7*, 294–296.
[51] K. Hayashi, H. Akutsu, H. Ozaki, H. Sawai, *Chem. Commun.* **2004**, 1386–1387.
[52] B. Yan, H. Zhang, S. Wang, J. Ni, *J. Photochem. Photobiol. A* **1998**, *116*, 209–214.
[53] N. J. Turro, *Modern Molecular Photochemistry*, Benjamin/Cummings, Menlo Park, **1978**.

Received: July 20, 2006
Published Online: November 3, 2006

